Supplementary Information for

An integrated low phase noise radiation-pressure-driven optomechanical oscillator chipset

Xingsheng Luan,[1,*] Yongjun Huang,[1,2,*] Ying Li,[1] James F. McMillan,[1] Jiangjun Zheng[1], Shu-Wei Huang[1], Pin-Chun Hsieh[1], Tingyi Gu[1], Di Wang,[1] Archita Hati,[3] David A. Howe,[3] Guangjun Wen[2], Mingbin Yu[4], Guoqiang Lo[4], Dim-Lee Kwong[4], and Chee Wei Wong,[1,*]

[1]*Optical Nanostructures Laboratory, Columbia University, New York, NY 10027, USA*

[2]*Key Laboratory of Broadband Optical Fiber Transmission & Communication Networks, School of Communication and Information Engineering*

University of Electronic Science and Technology of China, Chengdu, 611731, China

[3]*National Institute of Standards and Technology, Boulder, CO 80303, USA*

[4]*The Institute of Microelectronics, 11 Science Park Road, Singapore 117685, Singapore*

**Author e-mail address: xl2354@columbia.edu, yh2663@columbia.edu; cww2104@columbia.edu*

I. Chip layout and experiment setup

The chip layout is shown in Figure S1. For compactness on the CMOS chip, we placed our integrated OMO as center symmetric pairs. Here the inverse oxide taper coupler is shown in red on both input/output coupling sides and the silicon waveguide is shown in blue. The Ge detector is shown in dark purple, with the electrodes, vias and contact pads labelled in purple outline. The TE polarized light (designed at 1550 nm) is first focused into a low-loss oxide coupler by free-space lens and then coupled into the silicon waveguide before reaching the slot-type PhC cavity. In order to achieve maximum coupling from oxide coupler to the OMO, a taper is introduced at silicon waveguide to slot PhC waveguide interface. For the coupling between waveguide and cavity, different designs are included such as direct tunneling coupling as shown in Figure 1c in main text and side-coupling shown in Figure S1d below. The transmitted light is then split into two paths; one into the integrated Ge detector and the other coupled out from the inverse oxide coupler to a free-space lens for external detector monitoring.

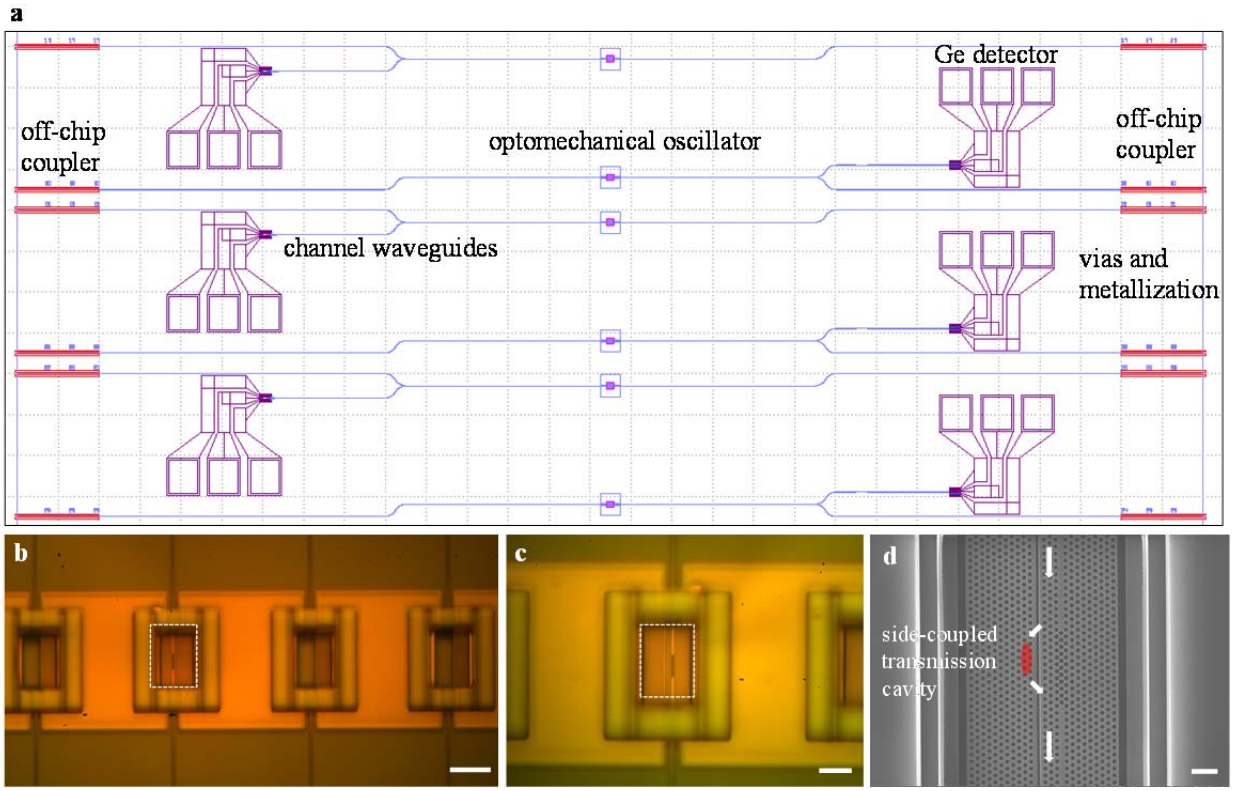

Figure S1 | Layout and nanofabrication results of the integrated OMO chipset. a, Overview layout within chipset. **b,** Optical image of nanofabricated OMOs. Scale bar: 30 μm. **c,** Optical image of nanofabricated OMO. Scale bar: 15 μm. **d,** SEM of OMO variations, with side-coupled tunneling transmission. Scale bar: 2 μm.

A simplified experimental setup is shown in Figure S2. Here the tunable laser (Santec TSL 510, Type C, 1500-1630 nm) first goes through a C-band erbium-doped fiber amplifier (EDFA), to achieve optical amplification if needed, such as for observing the higher order harmonics. For typical OMO operations, the EDFA is removed from the setup. Since our PhC cavity is designed for TE polarization, the fiber polarization controller and a bulk polarizer is used to eliminate the TM component of the input laser. At the output transmission, we use a slow detector (Thorlabs PDA10CS InGaAs Amplified Detector, bandwidth 17 MHz) and a fast detector (New Focus Model 1811 Low Noise Photoreceiver, bandwidth 125 MHz) to monitor the optical power and mechanical modulation on output field respectively. The electrical signal from Ge detector is measured from a RF probe (Picoprobe GSG-100-P, GGB Industries, Inc.) on the aluminum pads, as shown in Figure S2. To characterize the optomechanical coupling rate, an electro-optic phase

modulator (EOM; Covega Mach-10 10G phase modulator) is added to generate phase modulation on the input light. The external frequency reference is a tunable signal generator (Stanford Research System, Model SG384, DC-4.5 GHz).

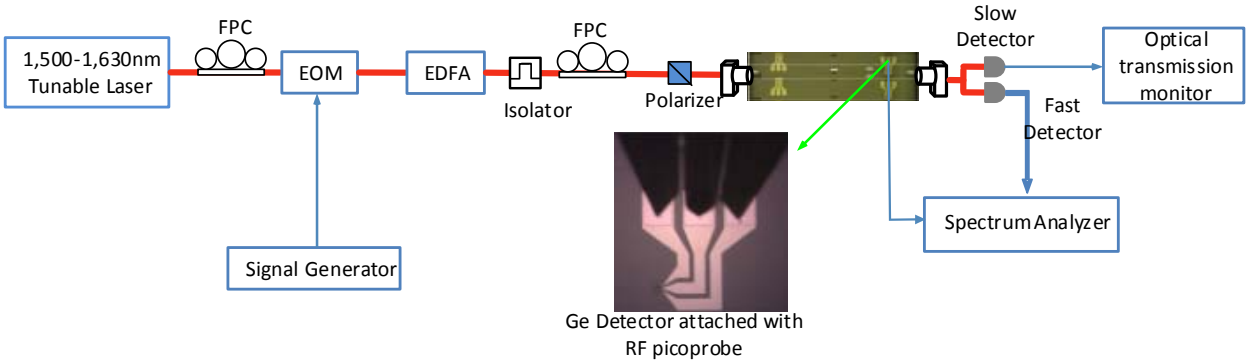

Figure S2 | Simplified experimental setup for the optical transmission and mechanical resonance measurements of the integrated OMO. A tunable semiconductor diode laser drives the OMO, with capabilities of external phase-modulation injection locking, optical amplification if needed, and simultaneous RF spectral analysis, phase noise analysis, and optical intensity transmission monitoring. The RF probes on the integrated Ge detector are illustrated in the optical image.

II. Ge detector design and characterization

The Ge detector is in a vertical *p-i-n* configuration, as shown in Figure S3. Such vertical *p-i-n* configuration enables low leakage current [S1], important for increasing signal to noise ratio. The *p*+ and *n*+ junctions are formed on Si and Ge regions respectively and are separated by an intrinsic Ge absorbing layer with thickness 500 nm. The vertical *p-i-n* has a width 4 μm and length 25 μm. Previous optical simulation shows such dimensions can efficiently absorb more than 80% of the incident light traveling in the waveguide [S1].

To fully characterize the performance of Ge detector, we first measured its DC response, as shown in Figure 2a in main text, which indicates a typical diode characteristic. The dark current is measured to be 500 nA at -1 V bias, while 1 μA is typically considered as the upper limit for a high-bandwidth design [S1]. Responsivity is another important parameter that characterizes the detector efficiency. For the Ge detector, we measured the responsivity with varying bias voltage. At zero bias (photovoltaic mode), the responsivity is almost 0.58 A/W. Increasing the reverse

bias (photoconductive mode) increases the responsivity of the detector. At -1 V bias, the responsivity of detector is saturated and reaches a maximum value of 0.62 A/W.

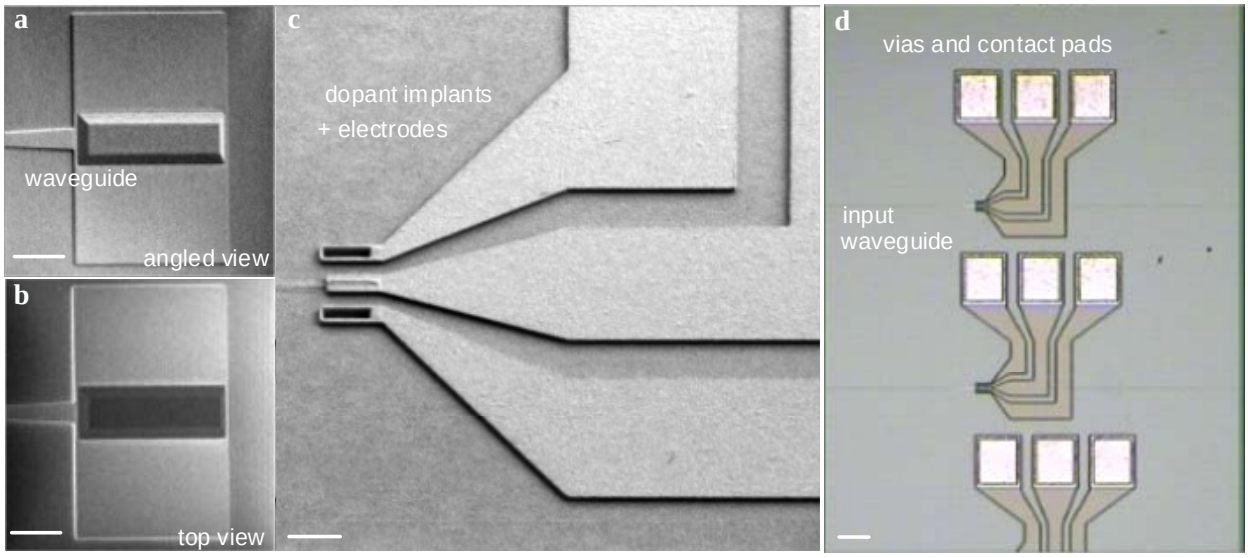

Figure S3 | The SEM images of the integrated Ge detector. a, Angled view. Scale bar: 10 μm **b**, Top view. Scale bar: 10 μm. **c**, Details of dopant implants and electrodes. Scale bar: 25 μm. **d**, Optical image of two Ge detectors with 25 μm and 50 μm lengths. Scale bar: 100 μm.

The frequency response of Ge detector is characterized by a lightwave component analyzer (LCA; Agilent 8703A, 1550nm, 0.13 to 20GHz) with the setup shown in Figure S4. Here the laser source from the LCA is modulated by a built-in modulator which is synchronized with its electrical measurement component. The frequency response of Ge detector under different bias voltage is shown in Figure 2b of the main text, a 9 GHz bandwidth at zero bias and 18.5 GHz at -1 V bias. Theoretically, the bandwidth is determined by

$$f_{3dB} = \sqrt{\frac{1}{1/f_{transit}^2 + 1/f_{RC}^2}}, \tag{S-1}$$

where

$$f_{transit} = \frac{0.45\upsilon_{sat}}{t_{i-Ge}} \text{ and } f_{RC} = \frac{1}{2\pi RC} \tag{S-2}$$

are the frequencies from the carrier transit time under saturation and the cutoff frequency of the capacitor formed by *p-i-n* junction, respectively. At zero bias, calculations indicate the bandwidth of the detector is limited by the cutoff frequency of the *p-i-n* junction at 20 GHz.

However, the experimental measurements are lower than this possibly due to the large lattice mismatch with Si (~4.2%) or variations in the actual RC time constant [S1].

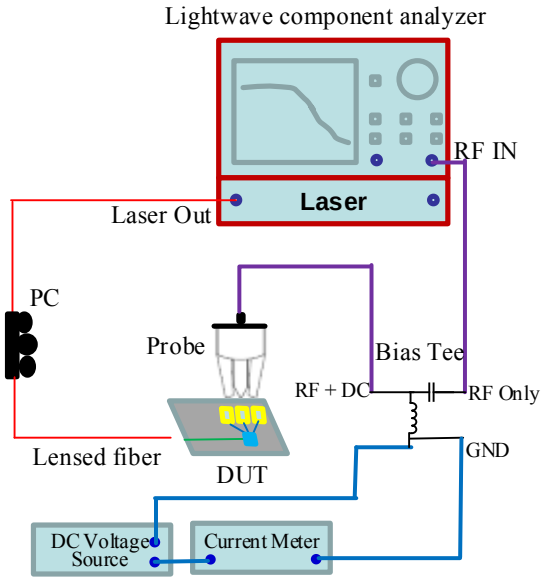

Figure S4 | Setup for characterizing the DC I-V and RF bandwidth properties of the integrated Ge detector. A RF probe contacts the metal pads as shown in Figure S2. Measurements are typically averaged over 10 scans, and the laser from lightwave component analyzer is synchronized with its built-in electronic measurement circuits to measure the RF response from on-chip Ge detector.

III. Estimation of intrinsic quality factor

To determine the intrinsic quality factor, we first determine the ratio of coupling rate and total loss rate κ_{ex}/κ. From the coupled-mode theory of the intracavity field [S2]

$$\dot{\alpha} = -\frac{\kappa}{2}\alpha + i\Delta\alpha + \sqrt{\frac{\kappa_{ex}}{2}}\alpha_{in}, \tag{S-3}$$

where α is the normalized intra cavity field amplitude in the rotating frame with laser frequency ω_L and $\Delta = \omega_L - \omega_{cav}$ is the laser detuning with respect to the cavity mode. The factor 2 for κ_{ex} is because our cavity is a bidirectional coupling standing-wave cavity [S2] and single direction is divided by 2. The steady state solution reads

$$\alpha = \frac{\sqrt{\frac{\kappa_{ex}}{2}}\alpha_{in}}{\frac{\kappa}{2} - i\Delta}. \tag{S-4}$$

Thus the transmitted light is given by

$$\alpha_{out} = i\sqrt{\frac{\kappa_{ex}}{2}}\alpha = \frac{i\frac{\kappa_{ex}}{2}\alpha_{in}}{\frac{\kappa}{2} - i\Delta}. \tag{S-5}$$

For the peak power,

$$\Delta = 0 \text{ and } \alpha_{out} = \frac{i\kappa_{ex}\alpha_{in}}{\kappa}. \tag{S-6}$$

Thus the output power and input power are related by

$$\frac{P_{out}}{P_{in}} = \frac{\hbar\omega_L\left|\alpha_{out}\right|^2}{\hbar\omega_L\left|\alpha_{in}\right|^2} = \left(\frac{\kappa_{ex}}{\kappa}\right)^2. \tag{S-7}$$

On the other hand, the intrinsic quality factor and loaded quality factor are also related by coupling rate and total loss rate

$$\frac{Q_L}{Q_i} = \frac{\omega_L/\kappa}{\omega_L/\kappa_i} = \frac{\kappa_i}{\kappa} = 1 - \frac{\kappa_{ex}}{\kappa}. \tag{S-8}$$

By inferring the input power before cavity and output power after cavity, we can determine the intrinsic quality factor. In this case, we also note that the accuracy is limited by the uncertainty of loss introduced by coupling from waveguide mode to slot guided mode due to effective index mismatching, which functions as an unknown attenuation before the cavity (and also after the cavity). To avoid this uncertainty, we infer κ_{ex}/κ by comparing the peak power with nearby waveguide mode which lies out of the photonic crystal band gap. For waveguide mode outside the photonic crystal band gap, the photonic crystal slab functions as a multimode interference structure and, for an upper bound on the Q_i estimate, we have $P_{\text{out,max}}/P_{\text{in}} \sim 1$ for the maximum transmitted wavelength. Thus, the ratio between cavity mode measured peak power and observed maximum transmitted power (as shown in Figure S5) equals the ratio $P_{\text{out}}/P_{\text{in}}$ for cavity mode, just like a side-coupled cavity.

From Figure S5, we get

$$\frac{P_{out}}{P_{in}} \approx \frac{0.02518}{0.05676} = 0.4436, \tag{S-9}$$

so

$$Q_i = Q_L\left(1 - \frac{\kappa_{ex}}{\kappa}\right)^{-1} = 213{,}195. \tag{S-10}$$

So the intrinsic quality factor is estimated to be ~ 2×10^5. Note that for the real case (even at maximum transmitted wavelength), $P_{out,max}/P_{in} < 1$, thus our above estimate is an upper bound for the intrinsic quality factor.

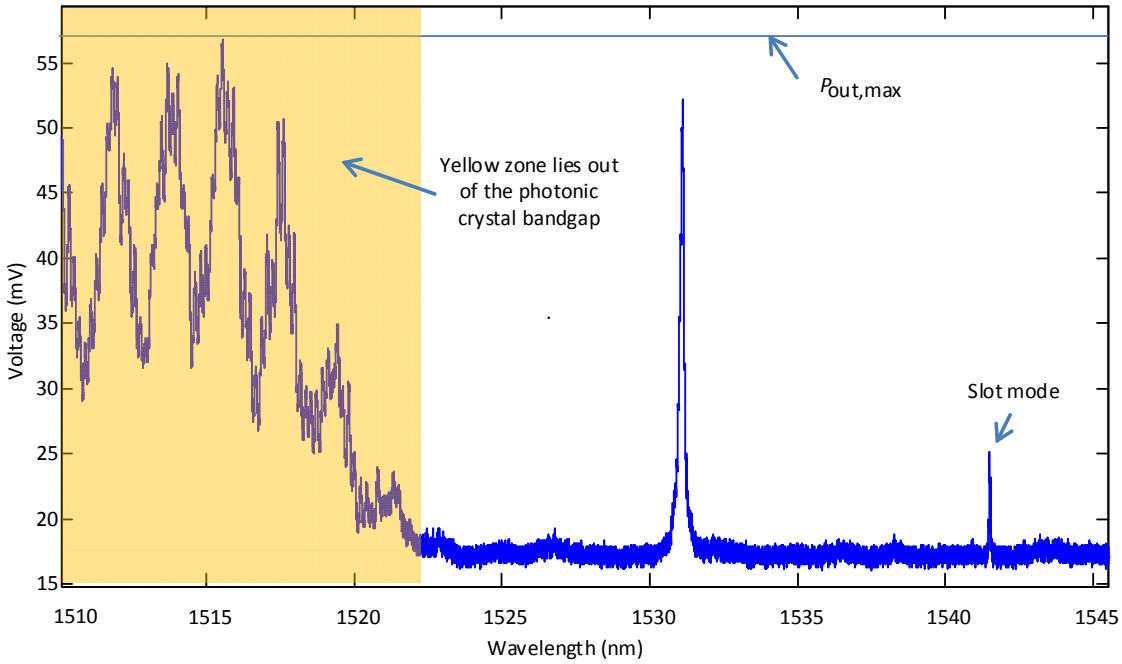

Figure S5 | Optical transmission in wide wavelength for the estimation of intrinsic quality factor. Wavelength in the yellow regime lies out of photonic bandgap and thus have larger transmission. The Fabry-Perot like transmission is due to internal reflections inside the waveguide.The level of maximum power and the slot mode is also identified in this plot.

IV. Determination of threshold power, optomechanical coupling rate, and loss channel

Power consumption is another important factor for a frequency reference. For our fully integrated OMO, the operating power is slightly above 200 μW. This is determined by the threshold power of parametric oscillation of the optomechanical resonator, where the effective linewidth becomes zero. When effective linewidth is zero, the change of linewidth due to optomechanical interaction is given by [S3,S4]

$$\Gamma_{opt} = g_0^2 \bar{n}_{cav} \left(\frac{\kappa}{(\Delta+\Omega_m)^2 + (\kappa/2)^2} - \frac{\kappa}{(\Delta-\Omega_m)^2 + (\kappa/2)^2} \right), \qquad \text{(S-11)}$$

where

$$\overline{n}_{cav} = \frac{P}{\hbar\omega_L}\frac{\kappa_{ex}}{\Delta^2 + (\kappa/2)^2}. \tag{S-12}$$

Let

$$\Gamma_{eff} = \Gamma_{opt} + \Gamma_m = 0, \tag{S-13}$$

we get

$$P_{th} = \frac{\Omega_m}{Q_m}\frac{\hbar\omega_L\left(\Delta^2 + (\kappa/2)^2\right)}{g_0^2\kappa_{ex}\kappa}\left(\frac{1}{(\Delta-\Omega_m)^2 + (\kappa/2)^2} - \frac{1}{(\Delta+\Omega_m)^2 + (\kappa/2)^2}\right)^{-1}. \tag{S-14}$$

Under weak retardation approximation (κ_{ex}>>Ω_m), we can simplify the expression above

$$P_{th} = \frac{\hbar\omega_L}{4g_0^2\kappa_{ex}\kappa Q_m}\frac{\left(\Delta^2 + (\kappa/2)^2\right)^3}{\Delta}. \tag{S-15}$$

Optimizing the detuning, the minimum threshold power is

$$P_{th} = \frac{27}{400\sqrt{5}}\frac{\hbar\omega_L}{g_0^2}\frac{\kappa^4}{Q_m\kappa_{ex}}, \tag{S-16}$$

and the corresponding detuning is

$$\Delta = \frac{\kappa}{2\sqrt{5}}. \tag{S-17}$$

Plugging experimental parameters into the expression above, we get $P_{th} \approx 127$ μW.

From Eq. (S-16), we get

$$P_{th} \propto \frac{1}{g_0^2 Q_m Q_o^3}. \tag{S-18}$$

This inverse dependence on mechanical Q_m, inverse-cubic dependence on the optical Q_o, and inverse-square dependence on vacuum optomechanical coupling rate make it desirable to have high mechanical/optical Q and large optomechanical coupling rate, to achieve low operating powers. In measurements the threshold power is characterized by slowing varying the input power and monitoring the mechanical spectrum, as shown Figure S6a to S6c.

The vacuum optomechanical coupling strength is determined by phase modulating the input light and compare the peak density power at OMO frequency and external modulated frequency in the spectrum domain [S5,S6]

$$g_0^2 = \frac{1}{2\bar{n}_{th}} \frac{\phi_0^2 \Omega_{\mathrm{mod}}^2}{2} \frac{S_{II}^{meas}(\Omega_m) \cdot \Gamma_m / 4}{S_{II}^{meas}(\Omega_{\mathrm{mod}}) \cdot ENBW}. \tag{S-19}$$

Here, ϕ_0 is the phase modulation amplitude and ENBW is abbreviated for effective noise bandwidth which is determined by the spectrum analyzer settings.

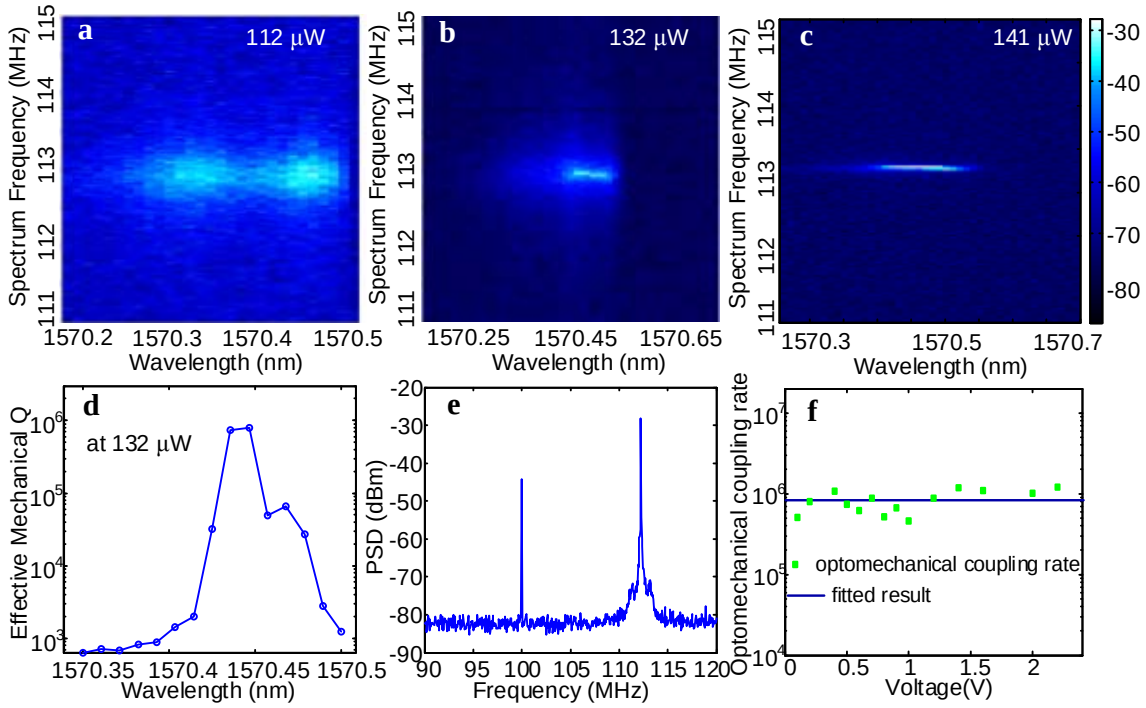

Figure S6 | Measured power spectrum and calculated mechanical *Q* and optomechanical coupling properties. a-c, 2D power spectra versus detuning wavelength and RF frequency at different dropped-in power values. **d,** Derived mechanical *Q* for the input power value shown in panel **b**. **e,** Power spectral density for the OMO signal and phase modulated signal. **f,** Calculated and fitted optomechanical coupling versus modulation voltage.

In experiment, we characterize the vacuum optomechanical coupling strength to be ~800 kHz (as shown in Figure S6e and S6f), which is smaller than numerical simulations of ~ 2.5 MHz. The discrepancy can be attributed to the deviations of the mechanical mode into two (slightly different) independent beams of the slot cavity and the mixing with other flexural modes of slot cavity. One example for the deviations is the splitting RF spectra obtained from out another chipset as shown in Figure S7.

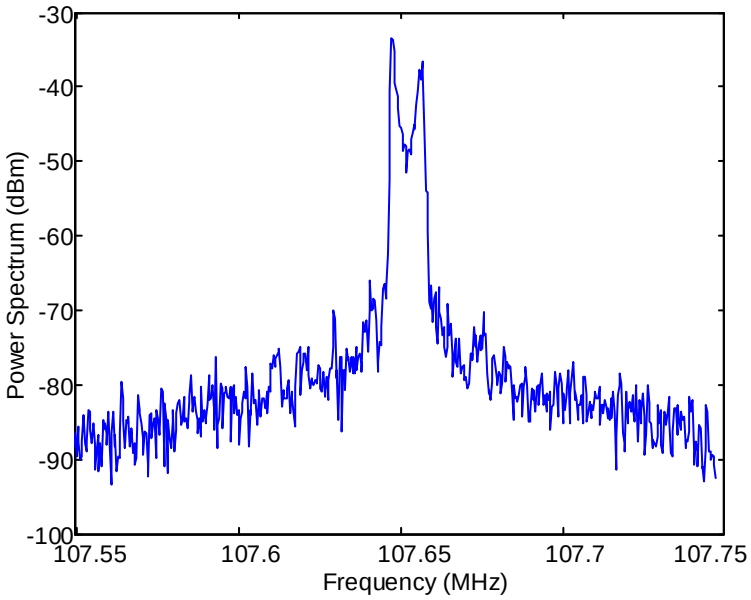

Figure S7 | Frequency splitting due to the deviations of the mechanical mode into two (slightly different) independent beams of the slot cavity.

In addition, several other reasons are responsible for the power consumption. First, observed under the top infrared imaging camera, ~ 5 dB of input light is scattered when coupling from the input silicon waveguide to slot cavity, mainly due to the finite tunneling rate between the waveguide mode and the cavity mode (highlighted in yellow in Figure S8). The finite tunneling rate of desired mode can also be verified in the optical transmission spectrum. As shown in Figure S5, the transmission of another higher mode has much larger power transmitted, which is proportional to the coupling rate κ_{ex}. This is because the higher order mode has a wider field distribution which leads to large field overlap and thus coupling rate with waveguide field. Moreover, a larger slot width leads to a lower effective modal index, with more scattering from the high-index silicon input channel waveguide due to mode mismatch. The coupling loss can be reduced by introducing more adiabatic coupling schemes into the slot waveguide and the side coupling approaches. Taking account the loss in coupling into the cavity, the dropped in power $P_d = \sqrt{P_{in} P_{out}}$ will be more useful in experimental analysis.

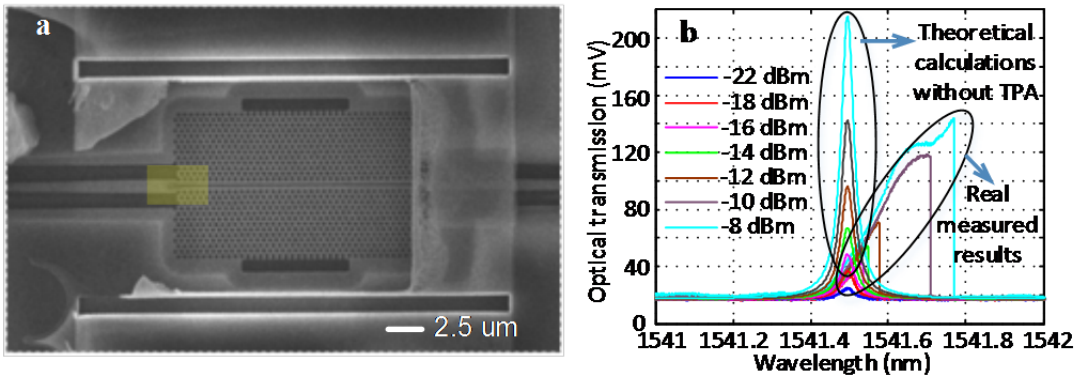

Figure S8 | SEM view and measured/calculated optical transmission for the characteristics of loss channels. a, SEM view of the OMO cavity. **b,** Measured versus calculated optical transmission.

When input power becomes large, nonlinear absorptions, e.g., two photon absorption and free carrier absorption, become an important loss channel [S6, S7]. As an example, we measured the thermal optical bistability effect by slowly sweeping the wavelength from shorter wavelength to longer wavelength (10 nm/s) under different input laser powers, as shown in Figure S8b. Theoretical ideal transmission resonances without nonlinear absorption is also shown in Figure S8b.

V. Measurement of phase noise and theoretical model fits

The phase noise of our OMO is measured by using Agilent 5052A signal source analyzer replacing the spectrum analyzer in the setup shown in Figure S1. To satisfy typical input power levels for the Agilent instrument, the output of both external photodetector and integrated Ge detector should be amplified by low noise amplifier. In measurement, to identify the real phase noise of our OMO, the IF gain and correlation of the Agilent instrument for phase noise measurement are set as 50 dB and above 128, respectively. At such settings, the phase noise floor of the instrument is shown in Figure 4a in main text, which is sufficient for our OMO measurement. The phase noise properties of three signal sources are measured for comparison, including a reference clock directly generated by a tunable RF signal generator (Stanford Research System, Model SG384, DC-4.5 GHz), and the OMO signal detected by both the external photodetector and integrated Ge detector. An example of the measured results are illustrated in Figure 4a of the main text.

To demonstrate the contributions of drifts in stage positioning and optical coupling on the phase noise for the integrated Ge and external detectors. We measure and compare the phase noise results at different conditions as shown in Figure S9 for examples. Specially, the lowest green curve is measured with laser modulated by EOM and then directly detected by the external detector while the dark blue curve is measured by first coupling the EOM-modulated laser into chip and then coupled out and detected by external detector. Here, the laser frequency is tuned far away from the optical cavity resonance and thus the mechanical oscillation is not amplified. By comparing these two groups of data, we can clearly see the difference is from the phase noise contributions of the drifts in stage positioning and optical coupling. Moreover, from the curves (dark blue and red, or light blue and purple), we can see lower phase noise in the close-to-carrier offset for the integrated Ge detector, which can confirm the drifts in stage positioning and optical coupling at output also contribute the phase noises. We can also compare the injection locking phase noise curves (light blue and purple) with the off-resonance mode curves (dark blue and red) to know that ~5 dBc/Hz phase noises is from OMO.

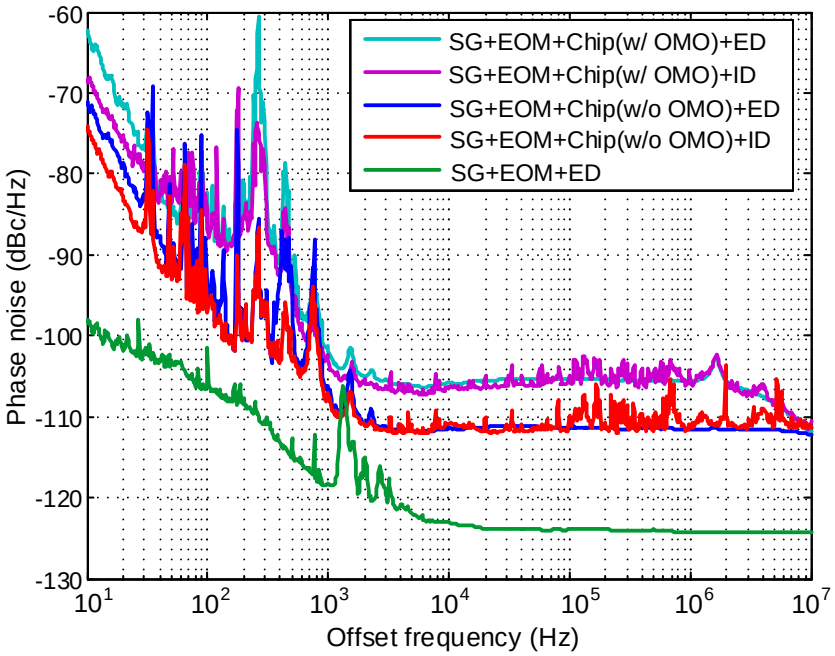

Figure S9 | Phase noises for demonstrations of the contributions of drifts in stage positioning and optical coupling. Here "ID" refer to integrated Ge detector and "ED" external detector.

Here we further theoretically fit the phase noise of OMO signal detected by the on-chip and off-chip detectors by using polynomial $\sum_{i=-4}^{0} b_i f^i$ (power law fitting theory) [S8]. Here b_i is obtained directly from the measured phase noise level at the different frequency offsets, and the corresponding b_i values obtained are: b_0 = -127 dBc/Hz, b_2 = -103 dBc/Hz, b_3 = -90 dBc/Hz, and b_4 = -78 dBc/Hz. As an example, the phase noise of our OMO with integrated Ge detector has a $1/f^4$ random walk frequency noise at lower offset related with mechanical shock, vibration, temperature, or other environmental effects, a $1/f^3$ flicker frequency noise in the range of 250 Hz to 800 Hz offset due to laser flicker phase noise, a $1/f^2$ white frequency noise in the range of 800 Hz to 15 kHz offset related to, and finally a $1/f^0$ white phase noise at higher frequency offsets. The $1/f^4$ noise is the result of slow environment noise processes, for example temperature fluctuation and instabilities from the measurement stage. This technical noise can be reduced by introducing temperature control and position feedback to the measurement stage, similar to the case for quartz oscillators. The $1/f^4$ may also arise from the diode laser used in our measurements. From Leeson model, the *1/f* flicker phase noise, common in semiconductors, can convert into $1/f^3$ noise at low frequency offset in a closed-loop oscillator. Further characterization of the laser noise can be attained by comparing the cases where OMO is driven by a low-noise fiber laser instead of a semiconductor diode lasers which have inherent carrier relaxation dynamics.

Moreover, the root-mean-square (RMS) timing jitter can also be converted from the measured phase noise results,

$$\text{RMS } J_{PER}\,|_{f_1 to f_c} = \frac{1}{2\pi f_c}\sqrt{2\int_{f_1}^{\nu_0} 10^{\frac{\mathscr{L}_\varphi(f)}{10}}\,df}\,. \tag{S-20}$$

where f_1 and ν_0 denote the start and stop (carrier frequency) of the integral. $\mathscr{L}_\varphi(f)$ is the measured phase noise in dBc/Hz. We calculated several RMS timing jitter values by stating different frequency f_1 as shown in Table 1.

Table 1 | Timing jitter for OMO measured by integrated Ge detector and external photodetector respectively. Otherwise denoted, units are in ps and shows the phase jitter per frequency segment, from the label frequency to the carrier.

Offset Frequency Range(Hz)	from 100 Hz	from 1 kHz	from 10 kHz
OMO (integrated Ge detector)	3.42	2.56	2.53
OMO (external photodetector)	10.01	0.69	0.40

The Allan deviation is calculated from the measured phase noise by

$$\sigma(\tau)=\sqrt{\sigma^2(\tau)}=\sqrt{\int_0^\infty \frac{4f^2L(f)}{f_c^2}\frac{\sin^4(\pi f\tau)}{(\pi f\tau)^2}df}\ . \qquad \text{(S-21)}$$

Here $\sigma^2(\tau)$ is the Allan variance and L is the phase noise of the oscillator. Furthermore, for better phase noise characteristics especially at close-to-carrier offset, injection locking technique can be used as a simple example to suppress the $1/f^4$ and $1/f^3$ noise. The setup is the same as Figure S1 and the electro-optic modulator used for injection locking is an amplitude modulator (JDS Uniphase, OC192 10 Gb/s Amplitude Modulator).

Supplementary references:

S1. Ang, K., Liow, T. & Yu, M. Low thermal budget monolithic integration of evanescent-coupled Ge-on-SOI photodetector on Si CMOS platform. *Sel. Top. Quantum Electron.* **16**, 106 (2010).

S2. Haus, H. A. *Waves and fields in optoelectronics.* (Prentice Hall, New Jersey, 1983).

S3. Aspelmeyer, M., Kippenberg, T. J. & Marquardt, F. Cavity Optomechanics. arxiv:1303.0733 (2013).

S4. Gorodetsky, M., Schliesser, A., Anetsberger, G., Deleglise, S. & Kippenberg, T. J. Determination of the vacuum optomechanical coupling rate using frequency noise calibration. *Opt. Express* **58**, 11 (2010).

S5. Gavartin, E. *et al.* Optomechanical coupling in a two-dimensional photonic crystal defect cavity. *Phys. Rev. Lett.* **106**, 203902 (2011).

S6. Yang, J., Gu, T., Zheng, J., Yu, M., Lo, G.-Q., Kwong, D.-L. & Wong, C. W., Radio-frequenc regeneration oscillations in monolithic high-*Q/V* heterostructured photonic crystal cavities. *Appl. Phys. Lett.* **104**, 061104 (2014).

S7. Yang, X., Husko, C. A., Yu, M., Kwong, D.-L. & Wong, C. W., Observation of femto-joule optical bistability involving Fano resonances in high-Q/V_m silicon photonic crystal nanocavities. *Appl. Phys. Lett.* **91**, 051113 (2007).

S8. Rubiola, E. *Phase noise and frequency stability in oscillators*. (Cambridge University Press, New York, 2008).